Time Domain Sampling of the Radial Functions in Spherical Harmonics Expansions

Nara Hahn, Frank Schultz, and Sascha Spors

***Abstract*—Spherical harmonics representations are widely adopted in applications such as analysis, manipulation, and synthesis of wave fields that are either captured or simulated. Recent studies have shown that, for broadband fields, a time domain representation of spherical harmonics expansions can benefit from computational efficiency and favorable transient properties. For practical usage, an accurate discrete-time modeling of spherical harmonics expansions is indispensable. The main challenge is to model the so called radial functions which describe the radial and frequency dependencies. In homogeneous cases, they are commonly realized as finite impulse response filters where the coefficients are obtained by sampling the continuous-time representations. This article investigates the temporal and spectral properties of the resulting discrete-time radial functions. The spectral distortions caused by aliasing are evaluated both analytically and numerically, revealing the influence of the distance from the expansion center, sampling frequency, and fractional sample delay. It is also demonstrated how the aliasing can be reduced by employing a recently introduced band limitation method.**

***Index Terms*—Radial filter, radial function, time-domain spherical harmonics expansion, time dependent wave field.**

I. Introduction

SPHERICAL harmonics expansion decomposes a wave field in terms of spherical basis solutions to the wave equation. The directional dependency of the wave field is described by spherical harmonics, whereas the radial dependency by spherical Bessel/Hankel functions [1, Section 7.2 and 8.2]. Spherical harmonics representations are suited for configurations with spherical symmetries, e.g. spherical source/sensor array, spherical radiator/scatterer [2], [3], thus have been widely adopted in spherical array signal processing [4]–[6]. Spherical harmonics en-/decoding of sound fields, known as Ambisonics, is a spatial sound recording and reproduction technique which has gained increasing attention in research and audio content production [7], [8].

In the literature, spherical harmonics expansions are predominantly expressed in the frequency domain, which the majority of signal processing techniques are based on [4], [6]. Frequency-domain representations are useful to describe the steady state of a wave field, but they provide little insight into the temporal structure which is crucial for broadband applications. Disregarding the time-domain characteristics might cause artifacts, e.g. temporal aliasing or pre-echoes. Moreover, frequency-domain implementations are typically more computationally intense as it requires the evaluation of the spherical Bessel/Hankel functions. This is even more critical in dynamic scenarios, where the expansion coefficients have to be regularly updated.

Time-domain representations of spherical harmonics expansion have drawn attention in electromagnetics research, motivated by the development of ultra-wideband systems operating with short pulse signals [9]–[11]. Analytical time-domain solutions are studied extensively for scattering problems [11]–[16]. The importance of temporal characteristics is also acknowledged in audio applications, where a bandwidth of about ten octaves is under consideration and the temporal structure is known to have significant impact on human perception of timbre and spaciousness [17]–[20]. Time-domain processing scheme was employed in spatial sound recording and reproduction techniques [21]–[27] where it was shown to be computationally efficient thus suited for real-time applications.

Time-domain processing of spherical harmonics expansions requires a stable and numerically accurate model of the radial functions. It is of practical interest to implement the radial functions as digital filters, where the spatio-temporal characteristics of the wave field are encoded. The so-called radial filters can be used to compute the wave field for an arbitrary source signal (cf. Fig. 1). This framework is quite versatile considering that most of the signals are available in digital form. Although not considered in this paper, wave fields can be also modeled with the source signal included [16]. This could be preferred if an analytical representation of the signal is known, e.g. Gaussian pulse.

There are two commonly used approaches for radial filter design. In the first approach, the radial filters are built based on their Laplace-domain representations characterized by complex poles and zeros [13], [21], [28]. By performing bilinear or impulse invariant transform [29, Section 7.1], infinite impulse response (IIR) filters are typically obtained. This method is frequently used for spherical microphone arrays [30], [31], sound field synthesis using circular/spherical loudspeaker arrays (higher-order Ambisonics with distance coding) [23], [32], and sound beam steering using loudspeakers baffled on a compact rigid surface [21], [22]. Although no explicit time-domain representation is used, the filtering process itself can be carried out in the time domain with a set of difference equations. If the

Manuscript received August 8, 2020; revised January 19, 2021 and March 26, 2021; accepted June 17, 2021. Date of publication June 28, 2021; date of current version August 11, 2021. The associate editor coordinating the review of this manuscript and approving it for publication was Dr. Weiyu Xu. *(Corresponding author: Nara Hahn.)*

The authors are with the Institute of Communications Engineering at the University of Rostock, 18119 Rostock, Germany (e-mail: nara.hahn@uni-rostock.de; frank.schultz@uni-rostock.de; sascha.spors@uni-rostock.de).

Digital Object Identifier 10.1109/TSP.2021.3092892

This work is licensed under a Creative Commons Attribution 4.0 License. For more information, see https://creativecommons.org/licenses/by/4.0/

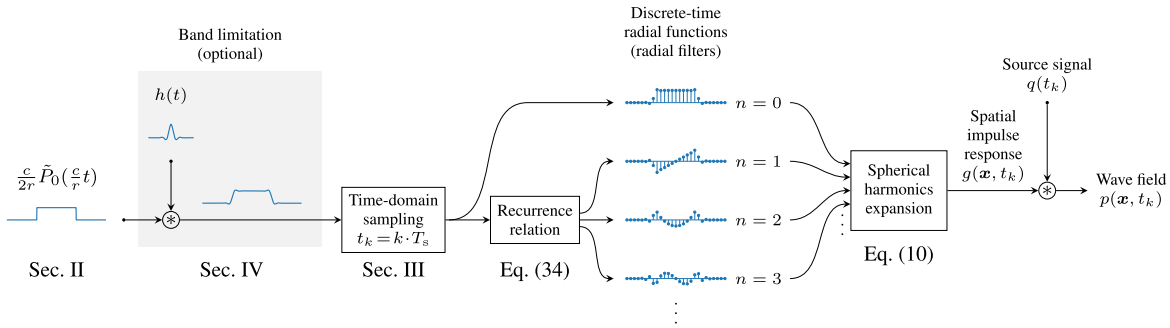

Fig. 1. Discrete-time modeling of a plane wave described by spherical harmonics expansion. The radial functions of different orders n are realized as FIR filters (Section III). The filter coefficients are obtained by sampling the respective continuous-time representations (Section II). Prior to time-domain sampling, an analytic low-pass filter can be applied in order to reduce aliasing (Section IV). The radial filters are linearly combined in the spherical harmonics expansion (10) yielding the spatial impulse response $g(\boldsymbol{x}, t_k)$ of the wave field at position $\boldsymbol{x}$. The wave field $p(\boldsymbol{x}, t_k)$ is obtained by filtering a source signal $q(t_k)$, i.e. $p(\boldsymbol{x}, t_k) = q(t_k) * g(\boldsymbol{x}, t_k)$ where $*$ denotes the convolution.

zeros and poles are properly calculated, the radial filter exhibits reasonable accuracy and the stability can be assured [32]. Since the zeros and poles are proportional to the distance from the expansion center, they can be pre-computed for a fixed radius and reused for differently scaled configurations [21, Ch. 3].

The focus of this paper is on the second approach which exploits analytical time-domain solutions to the wave equation [25], [33]–[35]. This is appropriate for homogeneous wave fields where the spatio-temporal impulse responses have a compact support in time. Since it is not trivial to model such impulse responses with IIR filters [35], [36], finite impulse response (FIR) filters are typically built by sampling the continuous-time radial functions. In sound field synthesis [25], [27], the loudspeaker driving functions are computed based on the discrete-time model of the target sound field using this approach. Recent active noise control techniques [37]–[39] also utilize FIR radial filters to model the sound field originating from outside the control region.

Despite the aforementioned advantages, currently available FIR radial filters have a caveat that has been relatively unexplored and somehow tolerated. Since the continuous-time radial functions are not strictly band limited, a time-domain sampling inevitably yields spectral aliasing [29, Ch. 4]. The numerical accuracy of a wave field is thus limited due to the resulting spectral distortion, which in turn might affect the performance of any application based on the wave field model. In the literature, severe distortion is often avoided by oversampling [14], [27], [37], [38] which benefits from the spectral decay of the radial functions at high frequencies.

The main goal of this article is to investigate the influence of aliasing on the accuracy of FIR-type radial filters. To the authors' best knowledge, this has not been studied in a comprehensive manner so far. The spatial dependency of the wave field model error was reported in [12], although not identified as aliasing. The remainder of this article is structured as follows. Based on the temporal and spectral properties of the radial functions (Section II), the aliasing distortion caused by time-domain sampling is examined (Section III-A). A closed form formula for aliasing energy is introduced (Section III-B), which reveals the effect of the harmonic order, radius and sampling frequency. Particular attention is paid to the impact of fractional sample delay which turns out to be detrimental on the spectral accuracy of the radial filters (Section III-C). As an improved radial filter design framework, a quasi-antialiasing strategy is introduced, which reduces the spectral distortion substantially without the need for oversampling (Section IV). New findings are all demonstrated by numerical simulations. The considered filter design and wave field modeling framework are outlined in Fig. 1. Further details are covered in the indicated sections.

Nomenclature Position vectors $\boldsymbol{x} = (r, \theta, \phi)$ are represented in spherical coordinates with r, θ and ϕ denoting the radius, colatitude and azimuth, respectively. Time is denoted by t and frequency by f where the latter is related to the angular frequency by $\omega = 2\pi f$. The modulus of a scalar is denoted by $|\cdot|$. The imaginary unit is denoted by i where $i^2 = -1$. The wave propagation speed is denoted by c and set to $343\ \mathrm{m/s}$ in numerical simulations.

II. Spherical Harmonics Expansion

The frequency and time-domain representations of the spherical harmonics expansion are reviewed in this section. Two frequently used source models, plane waves and spherical waves, are considered. The spectral and temporal properties of the continuous-time radial functions are examined which are of central importance for analyzing the aliasing spectra.

A. Frequency Domain

In the frequency domain, the spherical harmonics expansion of a plane wave propagating in the direction $\boldsymbol{n}_\mathrm{p} = (1, \theta_\mathrm{p}, \phi_\mathrm{p})$ reads [2, Eq. (6.175)]

$$e^{-i\frac{\omega}{c} r \cos\Theta_\mathrm{p}} = \sum_{n=0}^{\infty} \sum_{m=-n}^{n} 4\pi i^{-n} j_n(\tfrac{\omega}{c} r) Y_{nm}^*(\theta_\mathrm{p}, \phi_\mathrm{p}) Y_{nm}(\theta, \phi) \quad (1)$$

$$= \sum_{n=0}^{\infty} (2n+1) i^{-n} j_n(\tfrac{\omega}{c} r) P_n(\cos\Theta_\mathrm{p}) \quad (2)$$

where $Y_{nm}(\cdot,\cdot)$ denote the complex spherical harmonics, and $P_n(\cdot)$ the Legendre polynomials. The spherical Bessel functions of the first kind $j_n(\cdot)$ describe the radial and frequency

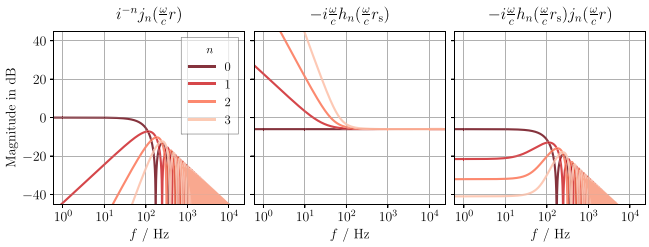

Fig. 2. Frequency-domain radial functions ($n = 0, \ldots, 3$). Left: plane wave (2). Right: spherical wave (3) with $r = 1$, $r_\mathrm{s} = 2$. Center: $-i\frac{\omega}{c} h_n(\frac{\omega}{c} r_\mathrm{s})$.

dependencies. The angle between $\boldsymbol{n}_\mathrm{p}$ and the evaluation point $\boldsymbol{x} = (r, \theta, \phi)$ is denoted by Θ_p. The addition theorem of the spherical harmonics is exploited in the second equality [40, Eq. (14.18.2)]. The time harmonic term $e^{i\omega t}$ is omitted.

The spherical harmonics representation of an omnidirectional point source located at $\boldsymbol{x}_\mathrm{s} = (r_\mathrm{s}, \theta_\mathrm{s}, \phi_\mathrm{s})$ reads [2, Eq. (8.22)]

$$\frac{e^{-i\frac{\omega}{c}R}}{4\pi R} = \frac{-i\frac{\omega}{c}}{4\pi} \sum_{n=0}^{\infty} (2n+1) j_n(\tfrac{\omega}{c} r_\wedge) h_n(\tfrac{\omega}{c} r_\vee) P_n(\cos\Theta_\mathrm{s}), \tag{3}$$

where $h_n(\cdot)$ denotes the spherical Hankel functions of the second kind. The Euclidean distance between the point $\boldsymbol{x}$ and $\boldsymbol{x}_\mathrm{s}$ is denoted by R and the angle between $\boldsymbol{x}$ and $\boldsymbol{x}_\mathrm{s}$ by Θ_s. The smaller and the greater between $\{r, r_\mathrm{s}\}$ are denoted by $r_\vee$ and $r_\wedge$, respectively. Equation (3) constitutes an interior expansion for $r < r_\mathrm{s}$ and an exterior expansion for $r > r_\mathrm{s}$ [2, Section 6.7 and 6.8].

Notice that the angular basis functions described by the spherical harmonics or the Legendre polynomials are frequency-independent, whereas the radial functions, $j_n(\cdot)$ and $h_n(\cdot)$, depend on ω. In the following, the spectral characteristics of the radial funtions in (2) and (3) are examined.

From the small argument approximations ($\omega \to 0$) of $j_n(\cdot)$ and $h_n(\cdot)$ [40, Eq. (10.52.1) and (10.52.2)], it follows that

$$j_n(\tfrac{\omega}{c} r_\wedge) \sim \frac{(\frac{\omega}{c} r_\wedge)^n}{(2n+1)!!} \tag{4}$$

$$-i\tfrac{\omega}{c} h_n(\tfrac{\omega}{c} r_\vee) \sim \frac{(2n-1)!!}{r_\vee \cdot (\frac{\omega}{c} r_\vee)^n}, \tag{5}$$

where !! denotes double factorial. At $\omega = 0$, the nth-order spherical Bessel function exhibits an nth-order zero, whereas the term $-i\frac{\omega}{c} h_n(\frac{\omega}{c} r_\vee)$ an nth-order pole, cf. Fig. 2. The asymptotic behavior of the radial functions for point sources can be expressed as

$$-i\tfrac{\omega}{c} h_n(\tfrac{\omega}{c} r_\vee)\, j_n(\tfrac{\omega}{c} r_\wedge) \sim \frac{1}{2n+1} \frac{r_\wedge^n}{r_\vee^{n+1}}. \tag{6}$$

Thus, for $\omega \to 0$, the magnitude converges to a constant as illustrated in Fig. 2 (right). For $n > 0$, a system described by $-i\frac{\omega}{c} h_n(\frac{\omega}{c} r_\vee)$ is unstable due to the poles at $\omega = 0$. However, (6) shows that this low-frequency boost is canceled by the zeros of $j_n(\frac{\omega}{c} r_\wedge)$.

In a similar manner, the high-frequency characteristics can be examined with the large argument approximations ($\omega \to \infty$) [40, Eq. (10.52.3) and (10.52.4)],

$$j_n(\tfrac{\omega}{c} r_\wedge) \sim \frac{1}{\frac{\omega}{c} r_\wedge} \sin\left(\tfrac{\omega}{c} r_\wedge - \tfrac{n\pi}{2}\right) \tag{7}$$

$$-i\tfrac{\omega}{c} h_n(\tfrac{\omega}{c} r_\vee) \sim i^n \frac{e^{-i\frac{\omega}{c} r_\vee}}{r_\vee}. \tag{8}$$

As shown in Fig. 2, the envelope of the spherical Bessel function decays with a rate of -20 dB/decade at high frequencies, whereas the term $-i\frac{\omega}{c} h_n(\frac{\omega}{c} r_\vee)$ has a constant magnitude $\frac{1}{r_\vee}$. The high-frequency approximation of the radial functions for point source (3) thus reads

$$-i\tfrac{\omega}{c} h_n(\tfrac{\omega}{c} r_\vee) j_n(\tfrac{\omega}{c} r_\wedge) \sim i^n \sin\left(\tfrac{\omega}{c} r_\wedge - \tfrac{n\pi}{2}\right) \frac{e^{-i\frac{\omega}{c} r_\vee}}{\frac{\omega}{c} r_\wedge r_\vee}, \tag{9}$$

which decays with the same rate as the radial functions for plane waves, i.e. $j_n(\frac{\omega}{c} r_\wedge)$.

B. Time Domain

A broadband plane wave excited by a Dirac impulse $\delta(t)$ is represented as [40, Eq. (10.59.1)]

$$\delta\left(t - \tfrac{r}{c}\cos\Theta_\mathrm{p}\right) = \frac{c}{2r} \sum_{n=0}^{\infty} (2n+1) \tilde{P}_n(\tfrac{c}{r} t) P_n(\cos\Theta_\mathrm{p}) \tag{10}$$

where $\tilde{P}_n(\frac{c}{r} t) := \mathrm{rect}(\frac{c}{r} t)\, P_n(\frac{c}{r} t)$ denotes the Legendre polynomial windowed by a rectangle function defined as

$$\mathrm{rect}(\tfrac{c}{r} t) = \begin{cases} 1, & |\frac{c}{r} t| < 1 \\ \frac{1}{2}, & |\frac{c}{r} t| = 1 \\ 0, & |\frac{c}{r} t| > 1. \end{cases} \tag{11}$$

Thus, $\tilde{P}_n(\frac{c}{r} t)$ vanishes for $|t| > \frac{r}{c}$ and coincides with $P_n(\frac{c}{r} t)$ for $|t| < \frac{r}{c}$. The same expression can be found in [11, Eq. (17)] and [35, Eq. (1)]. Since the Legendre polynomials form an orthogonal basis set for $|t| < \frac{r}{c}$ [41, Section 12.3], (10) constitutes a Legendre series expansion of the Dirac delta function [40, Eq. (1.17.22)]. Note that $\tilde{P}_n(\frac{c}{r} t)$ are not uniquely defined at the jump discontinuities $|t| = \frac{r}{c}$ [42, Section 9.6]. Indeed, any finite values can be assigned without affecting the Fourier transform relationship of the time and frequency-domain radial functions [43, Ch. 4]. Here, the mean value of the left and right limits $\frac{1}{2}[\frac{c}{2r} \tilde{P}_n(\frac{c}{r} t_-) + \frac{c}{2r} \tilde{P}_n(\frac{c}{r} t_+)]$ is chosen for convenience.

The time-domain spherical harmonics expansion for a point source at $\boldsymbol{x}_\mathrm{s} = (r_\mathrm{s}, \theta_\mathrm{s}, \phi_\mathrm{s})$ reads [33, Eq. (9)]

$$\frac{\delta\left(t - \frac{R}{c}\right)}{4\pi R} = \frac{c}{8\pi r r_\mathrm{s}} \sum_{n=0}^{\infty} (2n+1) \tilde{P}_n\left(\frac{r^2 + r_\mathrm{s}^2 - (ct)^2}{2 r r_\mathrm{s}}\right) P_n(\cos\Theta_\mathrm{s}), \tag{12}$$

where again R is the Euclidean distance between $\boldsymbol{x}$ and $\boldsymbol{x}_\mathrm{s}$. The radial functions have a finite support of $\frac{|r_\mathrm{s} - r|}{c} < t < \frac{r_\mathrm{s} + r}{c}$. Unlike the frequency-domain representation (3), the interior ($r < r_\mathrm{s}$) and exterior ($r > r_\mathrm{s}$) cases need not to be considered

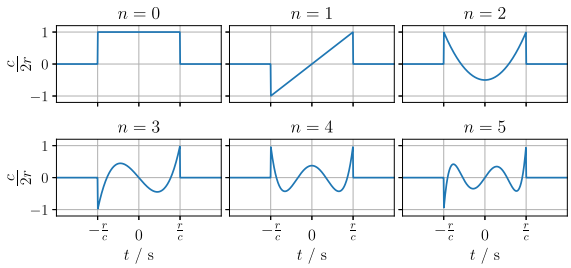

(a) Plane wave

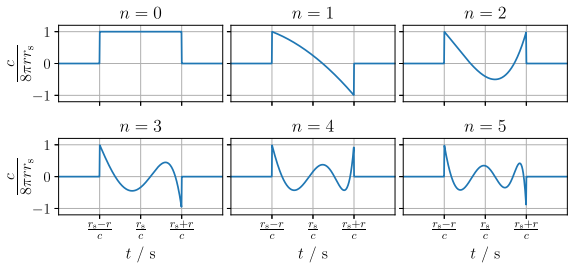

(b) Spherical wave

Fig. 3. Time-domain radial functions ($n = 0, 1, \ldots, 5$) for (a) plane wave (10) and (b) spherical wave (12) with $\frac{r_\mathrm{s}}{r} = 2$.

separately. The same expression can be found in [14, Eq. (15)] and [25, Eq. (34)]. An alternative representation is also available [33, Section III] where the time-domain radial function is given as the convolution of the inverse Fourier transforms $\mathcal{F}^{-1}\{j_n(\frac{\omega}{c}r_\wedge)\}$ and $\mathcal{F}^{-1}\{-i\frac{\omega}{c}r_\vee h_n(\frac{\omega}{c}r_\vee)\}$. A practical implementation is however not straightforward due to the unstable pole (at DC) of the spherical Hankel functions, cf. Fig. 2 (center).

The continuous-time radial functions for plane waves and spherical waves ($r_\mathrm{s} > r$) are depicted in Fig. 3(a) and 3(b), respectively. The non-causality of the plane wave radial functions (10) follows from the definition of the plane wave which passes the origin at $t = 0$. The spherical wave radial functions (12) are not symmetric due to the nonlinear argument of $\tilde{P}_n(\cdot)$. For a point source at far field ($r_\mathrm{s} \gg r$), the radial functions are found around $t = \frac{r_\mathrm{s}}{c}$, and its support ($|t - \frac{r_\mathrm{s}}{c}| < \frac{r}{c}$) is much smaller than $\frac{r_\mathrm{s}}{c}$. The squared propagation distance thus can be approximated with a Taylor series expansion (up to first order) at $t = \frac{r_\mathrm{s}}{c}$ [41, Section 5.6]

$$\begin{aligned}(ct)^2 &\approx r_\mathrm{s}^2 + (ct - r_\mathrm{s})(2r_\mathrm{s}) \\ &= 2r_\mathrm{s}ct - r_\mathrm{s}^2. \end{aligned} \tag{13}$$

The argument of $\tilde{P}_n(\cdot)$ in (12) thus can be written as

$$\begin{aligned}\frac{r^2 + 2r_\mathrm{s}^2 - 2r_\mathrm{s}ct}{2rr_\mathrm{s}} &= \frac{r}{2r_\mathrm{s}} + \frac{r_\mathrm{s}}{r} - \frac{ct}{r} \\ &\approx -\frac{c}{r}(t - \tfrac{r_\mathrm{s}}{c}), \end{aligned} \tag{14}$$

where $\frac{r}{2r_\mathrm{s}} \ll 1$ is omitted in the second row. As expected, the radial functions for a distant point source approximate the radial functions for a plane wave (10). Note that the far field radial functions are reversed and delayed. The delay $\frac{r_\mathrm{s}}{c}$ obviously corresponds to the propagation from the point source $\boldsymbol{x}_\mathrm{s}$ to the origin. The time reversal occurs because plane waves are defined with respect to the propagation direction $(\theta_\mathrm{p}, \phi_\mathrm{p})$ whereas point sources with respect to the direction of incidence $(\theta_\mathrm{s}, \phi_\mathrm{s})$. This mismatch is corrected by the angular dependent terms, $P_n(\Theta_\mathrm{p})$ in (10) and $P_n(\Theta_\mathrm{s})$ in (12). For $\Theta_\mathrm{p} = \pi - \Theta_\mathrm{s}$, they differ by a factor of $(-1)^n$ thus inverting the polarity for odd n which is equivalent to a time reversal for the plane wave radial functions, cf. Fig. 3(a). This follows from the reflection formula of the Legendre polynomials $P_n(-z) = (-1)^n P_n(z)$ [40, Eq. (14.7.17)].

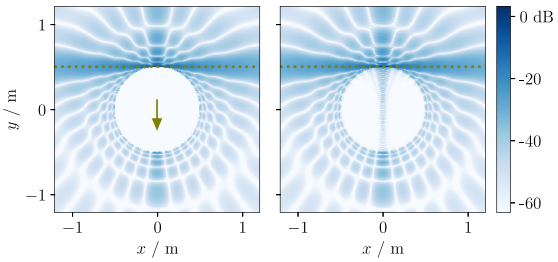

Fig. 4. A spatially band limited plane wave ($N = 15$, $\boldsymbol{n}_\mathrm{p} = (1, \frac{\pi}{2}, -\frac{\pi}{2})$, $c \cdot t = -0.5$ m). The wave field is computed from a truncated spherical harmonics expansion. Left: Time-domain expression (10). Right: Uniform sampling of the spectrum (2) followed by an inverse DFT (2^{14}, $|f| \leq 24$ kHz). The arrow (↓) and dotted line (···) indicate the propagation direction $\boldsymbol{n}_\mathrm{p}$ and the planar wavefront, respectively.

C. *Spatial Band Limitation*

In practice, a spherical harmonics expansion can be computed only up to a finite order ($0 \leq n \leq N$), where the maximum order N is referred to as the spatial bandwidth. A truncated expansion is a good approximation for $r < \frac{cN}{2\pi f}$ (or equivalently below a critical frequency $f_N < \frac{cN}{2\pi r}$) [3], [44]. It is suited for describing a wave field captured by a compact sensor array [4], [6]. Sound field synthesis techniques also often base on spatially band limited representations [5]. The accuracy of the synthesized sound field can be improved in a local target region by means of spatial band limitation and re-expansion [45]–[47].

Fig. 4 (left) is a snapshot of a planar wavefront with a spatial bandwidth of $N = 15$. The wave field is computed from the truncated version of (10). The smearing of the original wavefront (···) is due to the spatial band limitation, which corresponds to a two-dimensional convolution of the wave field with a sinc-like function in the (θ, ϕ)-domain [4], [48], [49]. The impulse responses of the same wave field is shown in Fig. 5 (—) for different positions. The time span of the impulse responses is identical, but the temporal structure differs substantially depending on Θ_p. Refer to [5, Section 2.2] and [35] for further discussions on the spatio-temporal structure of spatially band limited wave fields.

III. Time Domain Sampling and Spectral Aliasing

This section addresses the time-domain sampling of the radial functions. It is worth mentioning that a discrete-time modeling can be carried out by using the frequency sampling method [50, Section 7.3], where the frequency-domain representations are uniformly sampled and transformed into the

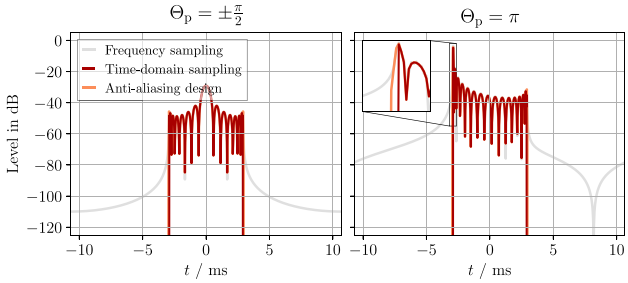

Fig. 5. Impulse responses of a plane wave with a finite spatial bandwidth ($N = 15$, $r = 0.5$, $f_s = 48$ kHz). — Time-domain sampling, — Anti-aliasing design ($L_{BLEP} = 6$, cf. Section IV), — Frequency sampling method (DFT length: 2^{10}, cf Section III).

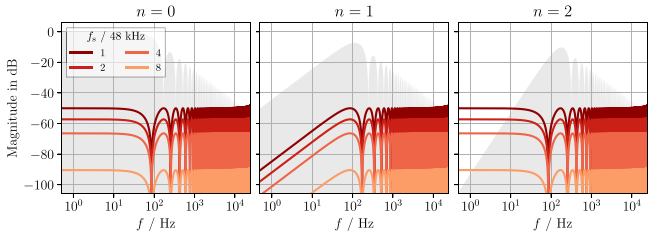

Fig. 6. Spectral distortions of the discrete-time radial functions obtained by trivial sampling ($r = 1$ m and $f_s = 48, 96, 192, 384$ kHz). The shaded area (■) indicates $20\log_{10}|i^{-n}j_n(\frac{\omega}{c}r)|$.

time domain by inverse discrete Fourier transform (DFT) [5, Section 2.2.2] [46]. This is computationally demanding since the spherical Bessel/Hankel functions have to be evaluated for every frequency bin. Another shortcoming of this approach is the occurrence of temporal artifacts. As depicted in Fig. 5 (—), the discrete-time radial functions have a long time support with slowly decaying tails, which is due to the ideally band limited spectrum and temporal aliasing. This has a direct impact on the spatio-temporal structure of the wave field, as shown in Fig. 4 (right).

Time-domain sampling, on the other hand, benefits from the limited time span of the radial functions. The time-domain radial functions need to be evaluated for much fewer sampling points. In addition, since the time-domain radial functions are described by nth-order polynomials (cf. Section II-B), the computational cost for each sample is much lower. These advantages, however, come at the cost of spectral impairments. A uniform sampling of the continuous-time radial functions, inevitably produces aliasing artifacts [29, Ch. 4]. This is because their spectra (2) and (3) are, although gradually decaying at high frequencies, not strictly band limited (cf. Fig. 2). In this section, the spectral distortions caused by aliasing are examined for plane wave radial functions. Most of the presented results also apply to spherical wave radial functions which have the same high-frequency characteristics (cf. Fig. 2). Radial filter design with anti-alias filtering will be discussed later in Section IV.

A. Aliasing Spectrum

Assume a uniform sampling of the continuous-time radial functions (10) with a sampling frequency of f_s. An ideal sampling is modeled by an impulse train [42, Section 11.2],

$$\sum_{k=-\infty}^{\infty} \delta(t - kT_s). \tag{15}$$

where $T_s = \frac{1}{f_s}$ denotes the sampling interval. Multiplying (15) to the nth radial function (10) yields

$$\sum_{k=-\infty}^{\infty} \frac{c}{2r}\tilde{P}_n(\tfrac{c}{r}kT_s)\cdot\delta(t - kT_s). \tag{16}$$

In the frequency domain, this corresponds to a convolution with an impulse train with period $\omega_s = 2\pi f_s$ [42, Eq. (11.33)],

$$\frac{2\pi}{T_s}\sum_{\mu=-\infty}^{\infty}\delta(\omega - \mu\cdot\omega_s). \tag{17}$$

The frequency response of the discrete-time radial function is thus a shifted sum of the original spectrum (2),

$$\frac{1}{T_s}\sum_{\mu=-\infty}^{\infty} i^{-n}j_n\left(\tfrac{r}{c}(\omega - \mu\cdot\omega_s)\right). \tag{18}$$

The spectral repetitions ($\mu \neq 0$) contribute to aliasing artifacts in the base band ($\mu = 0$). The term i^{-n} is included so that the spectrum is complex conjugate.

In order to examine the influence of the sampling rate on the spectral accuracy, discrete-time radial functions are computed for typical audio sampling frequencies $f_s = 48, 96, 192, 384$ kHz. Their frequency responses $\hat{H}_n(\omega)$ are compared with the original spectrum $H_n(\omega) = i^{-n}j_n(\frac{\omega}{c}r)$. For direct comparison, the discrete-time spectrum is scaled by T_s, cf. (18). The spectral distortions,

$$\mathcal{E}_n(\omega) = |H_n(\omega) - \hat{H}_n(\omega)|, \tag{19}$$

are depicted in Fig. 6 (—), where the shaded area (■) indicates the exact spectrum. As expected, the spectral distortion is strongest for $f_s = 48$ kHz and gradually decreases for higher sampling rates. Since higher sampling frequency increases the distance between the spectral repetitions, the spectral overlap (aliasing) is reduced. It also benefits from the decay of the spherical Bessel functions for large arguments, cf. (7). The improvements achieved by oversampling should not be generalized, since they are highly dependent on the chosen r and f_s. Although quite exceptional, it may occur that the distortion increases even for higher sampling rate. For $f_s = 48$ kHz, a slight boost is observed in the neighborhood of $f = \frac{f_s}{2}$. This is mainly attributed to the spectral repetition occurring at $f = f_s$. Notice from Fig. 6 that the aliasing spectra at high frequencies look alike for different orders n. This can be explained by the fact that the spherical Bessel functions exhibit the same large argument behavior which determines the aliasing spectrum. For $n = 1$, the distortion decreases at low frequencies. The same is observed for odd n in general. This is due to the odd symmetry of the FIR coefficients resulting in a null at $\omega = 0$. The spectral properties caused by certain symmetries of the radial functions

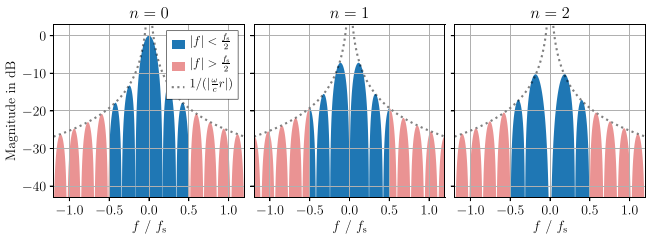

Fig. 7. Spectral components within (■) and beyond (■) the base band $|f| < \frac{f_s}{2}$ ($r = 1$ m, $f_s = 1$ kHz). The dashed line (▪▪▪▪) indicates the approximate decay, cf. (7). The frequency axis is normalized by f_s.

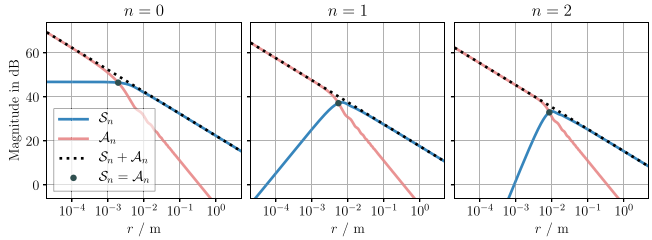

Fig. 8. Signal energy $\mathcal{S}_n$ (—) and aliasing energy $\mathcal{A}_n$ (—) for varying r. The dotted lines (▪▪▪▪) show the total energy $\mathcal{S}_n + \mathcal{A}_n = \frac{c}{r}\frac{\pi}{2n+1}$. The SAR_n can be read from the vertical distance between the two curves (— and —), which is 0 dB on their interaction (•). The sampling rate is $f_s = 48$ kHz.

are further discussed in Section III-C. For $n > 0$, the aliasing spectrum becomes increasingly dominant at low frequencies where the original spectrum rolls off.

B. Signal-to-Aliasing Ratio

Once the continuous-time radial functions are sampled, the spectral components outside the base band $|\omega| > \frac{\omega_s}{2}$ are aliased and overlap with those within $|\omega| < \frac{\omega_s}{2}$ resulting in spectral distortions [42, Section 11.3.2]. The respective components are depicted in Fig. 7 for $n = 0, 1, 2$. It can be seen that the spectral energy within $|\omega| < \frac{\omega_s}{2}$ (■) decreases for higher n, which is mainly due to the low frequency roll-off. The components beyond $\pm\frac{\omega_s}{2}$ (■) on the other hand are qualitatively similar for different n. As is well known from the sampling theory [42], higher ω_s includes more spectrum in the base band, and at the same time lowers the aliasing energy. Larger r also reduces the contribution of aliasing since the frequency axis is inversely scaled and thus more spectral energy lies within $|\omega| < \frac{\omega_s}{2}$. This is shown more rigorously through the following derivation.

The energy of the nth-order radial function can be expressed as an integral of the squared spectrum, [41, p. 734]

$$\frac{1}{2\pi}\int_{-\infty}^{\infty} |i^{-n} j_n(\tfrac{\omega}{c}r)|^2 \mathrm{d}\omega = \frac{c}{2r}\cdot\frac{1}{2n+1}. \tag{20}$$

The phase term i^{-n} has no effect on the integral, thus omitted in the remainder. Evaluating the energy in the time domain yields the same result [40, Eq. (14.17.6)],

$$\int_{-\infty}^{\infty} \left|\frac{c}{2r}\tilde{P}_n(\tfrac{c}{r}t)\right|^2 \mathrm{d}t = \frac{c}{2r}\cdot\frac{1}{2n+1}, \tag{21}$$

confirming the Parseval's theorem [42, Section 9.8]. The energy in the base band ($|\omega| < \frac{\omega_s}{2}$) reads

$$\mathcal{S}_n = \frac{1}{2\pi}\int_{-\omega_s/2}^{\omega_s/2} |j_n(\tfrac{\omega}{c}r)|^2 \mathrm{d}\omega \tag{22}$$

$$= \mathcal{I}_n(\tfrac{\omega_s}{2}) - \mathcal{I}_n(-\tfrac{\omega_s}{2}) \tag{23}$$

where $\mathcal{I}_n(\cdot)$ is the anti-derivative of the integrand [51],

$$\mathcal{I}_n(\omega) := \frac{1}{2\pi}\int_{-\infty}^{\omega} |j_n(\tfrac{\omega}{c}r)|^2 \mathrm{d}\omega$$
$$= \frac{\omega\cdot(\frac{\omega}{c}r)^{2n}}{2^{2n+1}\,(2n+1)^3\,\Gamma(n+\frac{1}{2})^2} \cdot {}_2F_3\left(n+\tfrac{1}{2}, n+1; n+\tfrac{3}{2}, n+\tfrac{3}{2}, 2n+2, -(\tfrac{\omega}{c}r)^2\right) \tag{24}$$

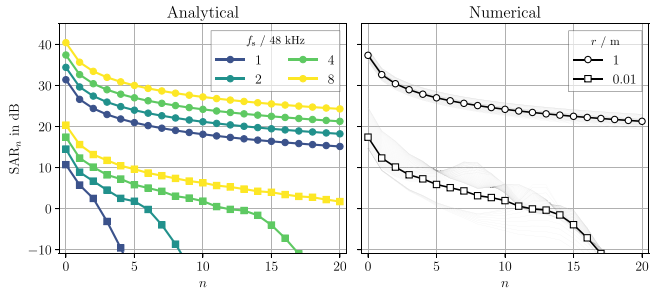

Fig. 9. Left: Analytical SAR_n (26) for $f_s = 48, 96, 192, 384$ kHz and $r = 0.01$ m (—■—), $r = 1$ m (—●—). Right: Numerical SAR_n (29) for $f_s = 192$ kHz and $\frac{r}{T_s} = -0.50, -0.49, \ldots, 0.49$ (▤). —○— and —□— indicate the numerical SAR_n based on averaged errors.

with $\Gamma(\cdot)$ denoting the Gamma function and ${}_qF_p(\cdot)$ the generalized hypergeometric function [40, Ch. 16]. The energy outside the Nyquist limit is thus

$$\mathcal{A}_n = \frac{1}{2\pi}\int_{-\infty}^{-\omega_s/2} |j_n(\tfrac{\omega}{c}r)|^2 \mathrm{d}\omega + \frac{1}{2\pi}\int_{\omega_s/2}^{\infty} |j_n(\tfrac{\omega}{c}r)|^2 \mathrm{d}\omega$$
$$= \frac{c}{2r}\cdot\frac{1}{2n+1} - \mathcal{S}_n. \tag{25}$$

By using these quantities, the signal-to-aliasing ratio (SAR) can be computed as

$$\mathrm{SAR}_n = \frac{\mathcal{S}_n}{\mathcal{A}_n} = \frac{1}{\frac{c}{2r}\frac{1}{2n+1}\frac{1}{\mathcal{S}_n} - 1}. \tag{26}$$

This is considered as an accuracy measure of each discrete-time radial function.

In Fig. 8, $\mathcal{S}_n$ (—) and $\mathcal{A}_n$ (—) are shown for varying r, where the sampling rate is $f_s = 48$ kHz. The total energy $\mathcal{S}_n + \mathcal{A}_n$ (▪▪▪▪) decays with $1/r$ (-10 dB for every tenfold increase of r) which follows from (20). The SAR_n level can be read from the vertical distance between the two curves. Up to their intersection ($\mathrm{SAR}_n = 0$ dB), the increasing rate of $\mathcal{S}_n$ is about $+6\cdot n$ dB per doubling of r. For larger radii, $\mathcal{S}_n$ gradually converge to the line $\frac{c}{2r}\frac{1}{2n+1}$ and $\mathcal{A}_n$ decreases with almost a constant rate of -12 dB per doubling of the distance. This leads to an increase of SAR_n by $+6$ dB for every twofold increase of r.

Fig. 9 (left) shows the SAR_n for different orders n, radii r, and sampling frequencies f_s. It can be seen that the SAR_n decreases for higher n, implying that a higher sampling frequency is

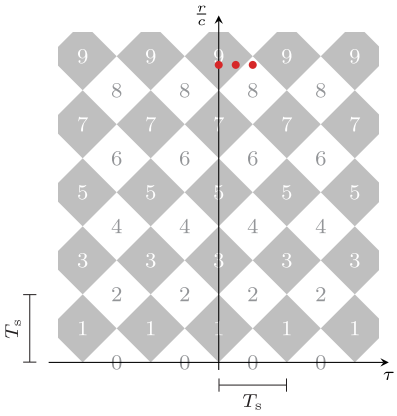

Fig. 10. Number of sampling points within $|t-\tau| < \frac{r}{c}$ as a function of τ and $\frac{r}{c}$ (cf. (28)). The diagonal length of each diamond is T_s. The red dots (•) correspond to the examples shown in Fig. 11 ($\frac{r}{cT_s} \approx 4.373$, $\frac{\tau}{T_s} = 0, 0.25, 0.5$).

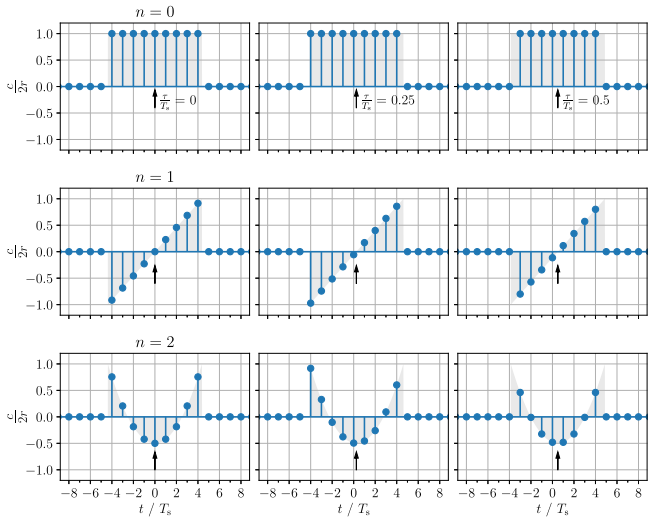

Fig. 11. Continuous (▒) and discrete-time (●) radial functions ($r = 1$ m, $f_s = 1.5$ kHz) for plane wave. The time shift $\frac{\tau}{T_s}$ is indicated by ↑. The length of the discrete-time signal is 9 samples for $\frac{\tau}{T_s} = 0, 0.25$ and 8 samples for $\frac{\tau}{T_s} = 0.5$.

required to achieve the same accuracy. The radius $r = 1$ m (-●-) is chosen such that SAR_n stays fairly above 0 dB. In this case, doubling the sampling frequency leads to an improvement of 3 dB in SAR_n. For $r = 0.01$ m (-■-), however, the SAR_n drops abruptly around 0 dB. The closer to the expansion center the more errors occur, which agrees with the observation in [12, Section 4]. Note that if r gets smaller, the time span of the radial function $2 \cdot \frac{r}{c}$ decreases. The distance between the zero crossings of the Legendre polynomials $\tilde{P}_n(\cdot)$ eventually becomes smaller than the sampling period and the oscillatory waveform cannot be sampled properly.

C. Influence of Fractional Sample Delay

In practice, it might be necessary to apply a time delay τ to the wave field, e.g. to turn (10) into a causal impulse response, to remove the leading zeros in (12), or to align multiple wave fields in time. The time delay shifts the individual radial functions accordingly,

$$\frac{c}{2r}\tilde{P}_n\left(\tfrac{c}{r}(t-\tau)\right). \tag{27}$$

In the continuous time domain, the group delay simply corresponds to a phase shift in the frequency domain $i^{-n} j_n(\frac{\omega}{c}r) e^{-i\omega\tau}$, thus leaving the magnitude response unaffected. However, the aliasing distortions exhibited by the discrete-time radial functions highly depend on the fractional part of $\frac{\tau}{T_s}$, as demonstrated below.

Recall that the time-domain radial functions (27) have a finite extent, which is now shifted to $|t-\tau| < \frac{r}{c}$. For a uniform sampling as in (16), the first (leftmost) nonzero sample appears at $t = T_s \cdot \lceil \frac{1}{T_s}(\tau - \frac{r}{c}) \rceil$ and the last (rightmost) sample at $t = T_s \cdot \lfloor \frac{1}{T_s}(\tau + \frac{r}{c}) \rfloor$, with $\lceil \cdot \rceil$ and $\lfloor \cdot \rfloor$ respectively denoting the ceil and floor function. The number of samples within this interval follows a nonlinear relation

$$M = \left\lfloor \tfrac{1}{T_s}(\tau + \tfrac{r}{c}) \right\rfloor - \left\lceil \tfrac{1}{T_s}(\tau - \tfrac{r}{c}) \right\rceil + 1, \tag{28}$$

which is depicted in Fig. 10. Even for constant $\frac{r}{c}$, the number of samples varies with τ, unless $\frac{r}{c}$ happens to be an integer or half-integer multiple of T_s. This is exemplarily shown in Fig. 11, where the sampled radial functions have different lengths.

Notice from Fig. 11 that the corresponding FIR filter may or may not have symmetric coefficients depending on $\frac{\tau}{T_s}$. For even n and an integer sample shift, both continuous (▒) and discrete-time (●) radial functions are even symmetric with respect to $t = \tau$ (↑). Since the number of sampling points within $|t-\tau| < \frac{r}{c}$ is odd, the discrete-time radial function can be considered as a linear-phase FIR filter of type-I [29, Section 5.7]. For a half integer sample shift (e.g. $\frac{\tau}{T_s} = 0.5$), the radial functions have even number of samples thus constituting a type-II linear-phase FIR filter. For other fractional sample shifts, the discrete-time radial functions are not symmetric and thus exhibit nonlinear phase responses. In Fig. 11 (top center), the 0th order radial function is still symmetric and corresponds to a linear-phase filter. However, since the sampled function is not centered at $t = \tau$, the group delay is incorrect. In a similar fashion, odd order radial functions can be interpreted as linear-phase FIR filters of type-III and IV for integer and half integer sample shifts, respectively.

In order to examine the spectral accuracy, the spectrum of the discrete-time radial function is compared with the exact spectrum $H_n(\omega) = i^{-n} j_n(\frac{\omega}{c}r) e^{-i\omega\tau}$. The time shift is varied from $\frac{\tau}{T_s} = 0$ to 0.5 with an increment of 0.1. The spectral distortions (19) are depicted in Fig. 12 . The magnitude spectra for $\frac{\tau}{T_s} = 0.6, 0.7, 0.8, 0.9$ are identical to those for $\frac{\tau}{T_s} = 0.4, 0.3, 0.2, 0.1$, respectively, and thus not shown. This is not the case for spherical waves because the continuous-time radial functions are not symmetric, cf. Fig. 3(b). It can be seen in Fig. 12 that the spectral accuracy varies quite substantially with τ. This is mainly attributed to the interference of the spectral repetitions (18), which now include the phase terms $e^{-i(\omega-\mu\omega_s)\tau}$. For $n = 0$, the distortion at $\omega = 0$ is either -50 dB or -68 dB. Since the 0th-order radial function is constant within

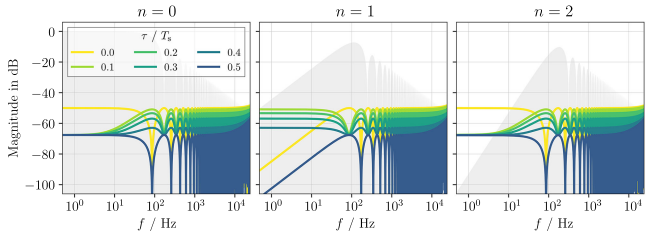

Fig. 12. Spectral distortions of discrete-time radial functions with varying time shifts ($\frac{\tau}{T_\mathrm{s}} = 0, 0.1, \ldots, 0.5$, $r = 1$ m, $f_\mathrm{s} = 48$ kHz). Exact spectrum.

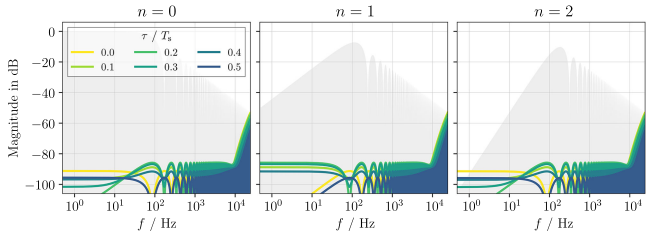

Fig. 13. Spectral distortion of discrete-time radial functions built with anti-aliasing filtering ($L_\mathrm{BLEP} = 6$). Compare with Fig. 12.

$|t| < \frac{r}{c}$, the DC offset is solely determined by its length, which is $M = 279$ for $\frac{\tau}{T_\mathrm{s}} = 0$ and $M = 280$ for $\frac{\tau}{T_\mathrm{s}} = 0.1, \ldots, 0.5$, cf. (28). The distortions for $n = 1$ (and also for other odd orders) decreases at low frequencies, if the radial functions are perfectly odd symmetric, i.e. $\frac{\tau}{T_\mathrm{s}} = 0, 0.5$. This is not the case for other fractional sample shifts where the distortion converges to a constant value. This explains the distinct behavior in Fig. 6 (center) where $\tau = 0$. It is worth noting that the relative strength between the distortions for different τ highly depends on the chosen parameters such as r and f_s. A half-integer sample shift does not always yield lower error as in Fig. 12.

The spectral variability is further examined in Fig. 9 (right), where the SAR_n is numerically evaluated as

$$\mathrm{SAR}_n \approx \frac{\|H_n(\omega)\|_2}{\|H_n(\omega) - \hat{H}_n(\omega)\|_2}, \tag{29}$$

with $\|\cdot\|_2$ denoting the l^2-norm along the frequency axis. $\hat{H}_n(\omega)$ is the DFT (2^{15}) of the discrete-time radial functions. The thin gray curves ( ) indicate the numerical SAR_n for $\frac{\tau}{T_\mathrm{s}}$ varying from -0.50 to 0.49 with an increment of 0.01. If the denominator (error norm) in (29) is averaged for the considered time shifts, the resulting SAR_n (,) is in a good agreement with the analytical value (,) in Fig. 9 (left). For $r = 1$ m, the spectral accuracy of each discrete-time radial function can be reasonably predicted by (26). For small r, however, the analytical SAR_n should be used with care, since the real (numerical) SAR_n has strong variations and (26) only follows the overall trend. The discrepancies are mainly due to the interference of the spectral repetitions which is not taken into account by the analytical SAR_n.

IV. Temporal Band Limitation

The spectral distortions observed in the previous section are primarily attributed to the discontinuities in the time domain. The waveform is comparably smooth in $|t| < \frac{r}{c}$, whereas the sharp transients occurring at $|t| = \frac{r}{c}$ exhibit an infinite bandwidth. In addition, since $|t| = \frac{r}{c}$ is generally not an integer multiple of the sampling period T_s, the exact timing of the discontinuities becomes ambiguous once the signal is sampled. The discrete-time radial functions are thus subject to group delay errors. As shown in Fig. 6, an oversampling can improve the accuracy to some extent. However, this comes at the cost of increased computational complexity which might be prohibitive in practical applications. This section presents a more efficient and effective approach, which is primarily introduced for musical sound synthesis [52]–[54]. The basic principle is to replace the discontinuities with smooth transients so that the spectrum outside the base band is sufficiently attenuated. In this way, the signal can be sampled with significantly reduced aliasing. Unlike conventional anti-alias filtering, the band-limitation has to be applied analytically to the continuous-time radial functions (cf. Fig. 1).

Consider the 0th-order radial function for plane wave (10) (rectangular pulse) which can be expressed as

$$\frac{c}{2r}\tilde{P}_0(\tfrac{c}{r}t) = \frac{c}{2r}\left(u(t + \tfrac{r}{c}) - u(t - \tfrac{r}{c})\right) \tag{30}$$

$$= \frac{c}{2r}\int_{-\infty}^{t}\left(\delta(\tau + \tfrac{r}{c}) - \delta(\tau - \tfrac{r}{c})\right)\mathrm{d}\tau, \tag{31}$$

with $u(\cdot)$ denoting the unit step function. Applying an anti-aliasing filter $h(t)$ to (31) replaces the Dirac delta functions with $h(t \pm \frac{r}{c})$,

$$\frac{c}{2r}\tilde{P}_0(\tfrac{c}{r}t) * h(t) = \frac{c}{2r}\int_{-\infty}^{t}\left(h(\tau + \tfrac{r}{c}) - h(\tau - \tfrac{r}{c})\right)\mathrm{d}\tau, \tag{32}$$

where $*$ is the time-domain convolution. The continuous-time filter $h(t)$ should suppress the spectrum outside the Nyquist limit and also serve as a fractional delay filter [55]. In this way, the transients introduced by the unit step functions in (30) can be smoothed. In the literature, the running integral of the filter $\int_{-\infty}^{t} h(\tau)\mathrm{d}\tau$ is referred to as the band-limited step (BLEP) function and its difference with the unit step function as the BLEP residual [53], [54],

$$\alpha(t) = \int_{-\infty}^{t} h(\tau)\mathrm{d}\tau \; - \; u(t). \tag{33}$$

As proposed in [53], any jump discontinuity can be smoothed out by adding a properly shifted and scaled BLEP residual onto the original signal. The 0th-order radial function with a limited bandwidth is shown in Fig. 14. In comparison with Fig. 11, the radial functions have smooth transients that properly model the non-integer delays.

This approach has been studied extensively in audio for the digital emulation of analog synthesizer sounds, e.g. square waves and sawtooth waves [52]–[54], [56]. The sampling of the 0th-order radial function $\tilde{P}_0(\cdot)$ is indeed very similar to the square wave case which has the same spectral decay. A distinctive difference is that the signal generated by a virtual analog synthesizer is intended for direct listening, whereas the

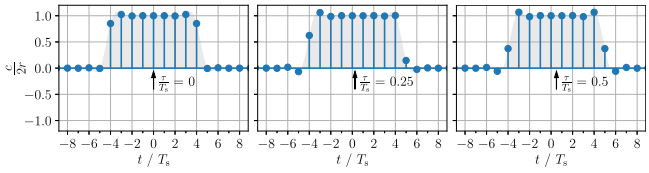

Fig. 14. Band-limited radial function for plane wave ($n = 0$, $r = 1$ m, $f_s = 1.5$ kHz, $\frac{\tau}{T_s} = 0, 0.25, 0.5$). The discrete-time radial function ( ) is obtained by sampling the low-pass filtered radial function ( ). The latter is derived by using the ideal BLEP funcion (35) windowed by a Kaiser-Bessel window (8 samples, $\beta = 8.6$). Compare with Fig. 11 (top).

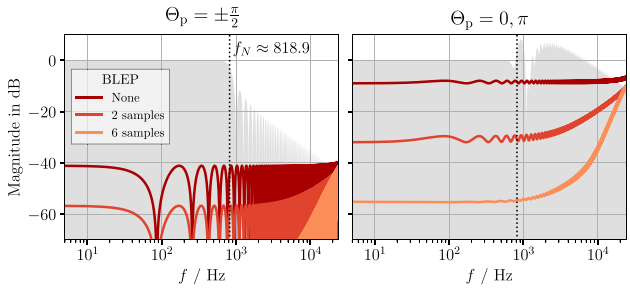

Fig. 15. Spectral distortion of a plane wave with a finite spatial bandwidth ($r = 1, N = 15, f_s = 48$ kHz, $f_N = \frac{cN}{2\pi r} \approx 818.9$ Hz). The shaded area ( ) indicates the exact spectrum and Θ_p denotes the angle between $\boldsymbol{x}$ and $\boldsymbol{n}_p$.

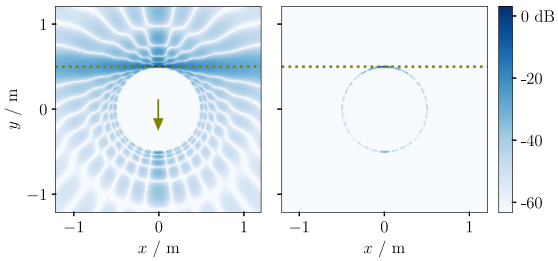

Fig. 16. Left: Spatially band limited plane wave ($N = 15, \boldsymbol{n}_p = (1, \frac{\pi}{2}, -\frac{\pi}{2})$, $c \cdot t = -0.5$ m) simulated based on a low-pass filtered representation ($f_s = 48$ kHz, $L_{\mathrm{BLEP}} = 6$, cf. Section IV). Right: The difference between the latter and the wave field without anti-alias filtering Fig. 4 (left). The arrow ( ) and dotted line ( ) indicate the propagation direction $\boldsymbol{n}_p$ and the wavefront of the original plane wave, respectively.

radial functions are linearly combined (10) and used as a filter (cf. Fig. 1), e.g. for auralization.

Once a band-limited 0th-order radial function is obtained, the higher order radial functions can be computed by exploiting the recurrence relation of the Legendre polynomials [40, Eq. (14.10.3)],

$$(n+1)P_{n+1}(z) = (2n+1)zP_n(z) - nP_{n-1}(z). \qquad (34)$$

This is equally applicable to spherical wave radial functions which are also represented by Legendre polynomials, cf. (12).

For demonstration purpose, the BLEP function is derived from the sinc function $h(t) = \mathrm{sinc}(f_s \cdot t) := \frac{\sin(\pi f_s t)}{\pi f_s t}$ which constitutes an ideal low-pass filter. A closed form BLEP function is known for this filter [40, Eq. (6.2.10)][56, Eq. (10)],

$$\int_{-\infty}^{t} \mathrm{sinc}\left(f_s \cdot (\tau \pm \tfrac{r}{c})\right) \mathrm{d}\tau = \frac{1}{2} + \frac{1}{\pi}\mathrm{Si}\left(\pi f_s \cdot (t \pm \tfrac{r}{c})\right) \qquad (35)$$

where $\mathrm{Si}(\cdot)$ denotes the sine integral function. The improved accuracy of the radial functions is shown in Fig. 13. The BLEP residuals are truncated to 6 samples and tapered by a Kaiser-Bessel window ($\beta = 8.6$) symmetrically with respect to $|t - \tau| = \pm\frac{r}{c}$ [57]. Compared with the radial functions evaluated in Fig. 12, a total of 12 samples are changed. Up to 10 kHz, the spectral distortion is reduced by more than 30 dB, which is comparable to an oversampling by a factor of 8 (cf. Fig. 6). The boost around the Nyquist frequency is still present but considerably attenuated. It is also possible to used this approach in combination with oversampling, which further reduces the distortion (not shown here).

The BLEP function discussed above is admittedly not the most practical choice, because is has to be truncated and windowed. As an alternative, BLEP functions can be built with piece-wise polynomials [56], [58]. The ideal band limitation is traded off against computational efficiency. Preliminary results can be found in [59], where BLEP functions based on Lagrange polynomials are used for radial filter design.

The improved discrete-time radial functions are now used to model a plane wave with a finite spatial bandwidth ($N = 15$) in the spherical harmonic domain (10). For anti-alias filtering, BLEP functions based on the sinc function with different lengths ($L_{\mathrm{BLEP}} = 2, 6$) are used. The spectral distortions of the wave field are depicted in Fig. 15 for a fixed radius and different angles. The influence of the spatial band limitation on the spectrum ( ) above the critical frequency $f_N = \frac{N}{2\pi r}$ can be seen. In spite of using the same radial functions, the overall spectral accuracy strongly depends on the angle relative to the direction of incidence (Θ_p), which determines how the individual radial functions in (10) are linearly combined. The benefit of employing the anti-aliasing method is apparent. Regardless of Θ_p, radial functions with less aliasing (larger L_{BLEP}) yield better result.

The impulse responses of the same wave field are depicted in Fig. 5 ( ). The result can be compared with the frequency sampling method ( ) and the time-domain design without anti-aliasing ( ). Notice that the BLEP residuals barely affect the temporal structure of the wave field. Contrary to the frequency sampling method, no temporal artifacts occur. The same is true for the spatial structure of the wave field, as shown in Fig. 16 (left). The difference between Fig. 16 (left) and Fig. 4 (left) is depicted in Fig. 16 (right), showing the components corresponding to the BLEP residuals.

V. Conclusion

This article addresses the problem of modeling spherical harmonics expansion of wave fields in the discrete-time domain. The radial basis solutions to the wave equation are realized as FIR filters based on their analytical representations in the continuous-time domain. The obtained radial filters constitute the spatio-temporal impulse responses of the individual spherical harmonic components which can be used in combination with a wide range of source signals.

A comprehensive treatment of uniformly sampled radial functions is presented, where the temporal and spectral properties are thoroughly investigated. It is shown that sampling without band limitation inevitably results in aliasing which impairs the frequency-domain accuracy. An analytical expression for signal-to-aliasing ratio is derived which can be used to predict the accuracy of each radial function in an approximate manner. Aliasing distortions for different scenarios are numerically evaluated, revealing the effect of harmonic order, radius, sampling frequency and, if present, time delay.

As demonstrated in Section IV, a more accurate discrete-time modeling is possible by using a band limitation method. This is particularly beneficial for small radii and high orders, where time discretization is more susceptible to aliasing artifacts. The order of the band limitation filter (BLEP length) can be optimized by considering the distortion level that is tolerable. In audio applications, this requires to examine the perceptual impact of aliasing, which remains for future study.

The presented work can be used to improve existing time-domain array signal processing techniques, e.g. sound field synthesis, active noise control. Also, array signal processing based on frequency domain representations can be reformulated in the time domain, thereby benefiting from computational efficiency and most importantly well-defined transients.

ACKNOWLEDGMENT

The authors wish to thank Franz Zotter for his invaluable suggestions.

REFERENCES

[1] P. M. Morse and K. U. Ingard, *Theoretical Acoustics*. New York, NY, USA: McGraw Hill, 1968.
[2] E. Williams, *Fourier Acoustics: Sound Radiation and Nearfield Acoustical Holography*. London, UK: Academic Press, 1999.
[3] N. A. Gumerov and R. Duraiswami, *Fast Multipole Methods for the Helmholtz Equation in Three Dimensions*. Oxford, UK: Elsevier, 2005.
[4] B. Rafaely, *Fundamentals of Spherical Array Processing*. Berlin, Germany: Springer, 2015.
[5] J. Ahrens, *Analytic Methods of Sound Field Synthesis*. Berlin, Germany: Springer, 2012.
[6] A. Kuntz, *Wave Field Analysis Using Virtual Circular Microphone Arrays*. Munich, Germany: Verlag Dr. Hut, 2009.
[7] M. A. Gerzon, "Periphony: With-height sound reproduction," *J. Audio Eng. Soc.*, vol. 21, no. 1, pp. 2–10, 1973.
[8] F. Zotter and M. Frank, *Ambisonics*. Cham, Switzerland: Springer, 2019.
[9] E. Heyman and A. Devaney, "Time-dependent multipoles and their application for radiation from volume source distributions," *J. Math. Phys.*, vol. 37, no. 2, pp. 682–692, 1996.
[10] A. Shlivinski, E. Heyman, and A. J. Devaney, "Time domain radiation by scalar sources: Plane wave to multipole transform," *J. Math. Phys.*, vol. 42, no. 12, pp. 5915–5919, 2001.
[11] S. A. Azizoglu, S. S. Koc, and O. M. Buyukdura, "Spherical wave expansion of the time-domain free-space dyadic green's function," *IEEE Trans. Antennas Propag.*, vol. 52, no. 3, pp. 677–683, Mar. 2004.
[12] S. A. Azizoglu, S. S. Koc, and O. M. Buyukdura, "Time domain scattering of scalar waves by two spheres in free-space," *SIAM J. Appl. Math.*, vol. 70, no. 3, pp. 694–709, 2009.
[13] L. Greengard, T. Hagstrom, and S. Jiang, "The solution of the scalar wave equation in the exterior of a sphere," *J. Comput. Phys.*, vol. 274, pp. 191–207, 2014.
[14] J. Li, D. Dault, and B. Shanker, "A quasianalytical time domain solution for scattering from a homogeneous sphere," *J. Acoust. Soc. Amer.*, vol. 135, no. 4, pp. 1676–1685, 2014.
[15] J. Li and B. Shanker, "Time-dependent Debye-Mie series solutions for electromagnetic scattering," *IEEE Trans. Antennas Propag.*, vol. 63, no. 8, pp. 3644–3653, Aug. 2015.
[16] P. Martin, "Acoustic scattering by a sphere in the time domain," *Wave Motion*, vol. 67, pp. 68–80, 2016.
[17] J. Blauert, *Spatial Hearing: The Psychophysics of Human Sound Localization*. Cambridge, MA, USA: MIT Press, 1997.
[18] H. Kuttruff, *Room Acoustics*. New York, NY, USA: CRC Press, 2016.
[19] B. C. Moore, *An Introduction to the Psychology of Hearing*. Leiden, The Netherlands: Academic Press, 1997.
[20] E. Zwicker and H. Fastl, *Psychoacoustics*. Berlin, Germany: Springer, 1999.
[21] H. Pomberger, "Angular and radial directivity control for spherical loudspeaker arrays," Master's thesis, Univ. Music Dramatic Arts, Graz, Austria, 2008.
[22] F. Zotter, "Analysis and synthesis of sound-radiation with spherical arrays," Ph.D. dissertation, Univ. Music Performing Arts, Graz, Austria, 2009.
[23] S. Spors, V. Kuscher, and J. Ahrens, "Efficient realization of model-based rendering for 2.5-dimensional near-field compensated higher order ambisonics," in *Proc. IEEE Workshop Appl. Signal Process. Audio Acoust.*, New Paltz, USA, Oct. 2011, pp. 61–64.
[24] S. Yan, H. Sun, X. Ma, U. P. Svensson, and C. Hou, "Time-domain implementation of broadband beamformer in spherical harmonics domain," *IEEE Trans. Audio Speech Lang. Process.*, vol. 19, no. 5, pp. 1221–1230, Jul. 2011.
[25] M. Poletti, T. D. Abhayapala, and P. D. Teal, "Time domain description of spatial modes of 2D and 3D free-space greens functions," in *Proc. Audio Eng. Soc. Conf.*, Guildford, UK, 2016.
[26] F. Winter, N. Hahn, and S. Spors, "Time-domain realisation of model-based rendering for 2.5D local wave field synthesis using spatial bandwidth-limitation," in *Proc. Eur. Signal Process. Conf.*, Kos, Greece, 2017, pp. 688–692.
[27] N. Hahn, F. Winter, and S. Spors, "2.5D local wave field synthesis of a virtual plane wave using a time domain representation of spherical harmonics expansion," in *Proc. 23rd Int. Cong. Acoust.*, Aachen, Germany, Sep. 2019, pp. 1132–1139.
[28] S. E. Field and S. R. Lau, "Fast evaluation of far-field signals for time-domain wave propagation," *J. Sci. Comput.*, vol. 64, no. 3, pp. 647–669, 2015.
[29] A. V. Oppenheim, R. W. Schafer, and J. R. Buck, *Discrete-Time Signal Processing*. Upper Saddle River, NJ, USA: Prentice Hall, 1999.
[30] R. Baumgartner, H. Pomberger, and M. Frank, "Practical implementation of radial filters for ambisonic recordings," in *Proc. Int. Conf. Spatial Audio*, 2011.
[31] S. Lösler and F. Zotter, "Comprehensive radial filter design for practical higher-order ambisonic recording," in *Proc. 41st German Annu. Conf. Acoust. (DAGA)*, 2015, pp. 452–455.
[32] N. Hahn and S. Spors, "Further investigations on the design of radial filters for the driving functions of near-field compensated higher-order ambisonics," in *Proc. 142nd Audio Eng. Soc. Conv.*, Berlin, Germany, 2017.
[33] O. M. Buyukdura and S. S. Koc, "Two alternative expressions for the spherical wave expansion of the time domain scalar free-space green's function and an application: Scattering by a soft sphere," *J. Acoust. Soc. Amer.*, vol. 101, no. 1, pp. 87–91, 1997.
[34] N. Hahn, F. Winter, and S. Spors, "Synthesis of a spatially band-limited plane wave in the time-domain using wave field synthesis," in *Proc. Eur. Signal Process. Conf.*, Kos Island, Greece, Aug. 2017, pp. 673–677.
[35] N. Hahn and S. Spors, "Time-domain representations of a plane wave with spatial band-limitation in the spherical harmonics domain," in *Proc. 45th German Annu. Conf. Acoust. (DAGA)*, Rostock, Germany, Mar. 2019, pp. 1434–1439.
[36] R. Baumgartner, "Time domain fast-multipole translation for ambisonics," Master's thesis, Univ. Music Dramatic Arts, Graz, Austria, 2011.
[37] H. Sun, T. D. Abhayapala, and P. N. Samarasinghe, "Time domain spherical harmonic analysis for adaptive noise cancellation over a spatial region," in *Proc. IEEE Int. Conf. Acoust., Speech, Signal Process.*, 2019, pp. 516–520.
[38] F. Ma, W. Zhang, and T. D. Abhayapala, "Reference signal generation for broadband ANC systems in reverberant rooms," in *Proc. Int. Conf. Acoust., Speech, Signal Process.*, 2018, pp. 216–220.
[39] F. Ma, W. Zhang, and T. D. Abhayapala, "Real-time separation of non-stationary sound fields on spheres," *J. Acoust. Soc. Amer.*, vol. 146, no. 1, pp. 11–21, 2019.

[40] F. W. J. Olver, D. W. Lozier, R. F. Boisvert, and C. W. Clark, *NIST Handbook of Mathematical Functions Handback*. New York, NY, USA: Cambridge Univ. Press, 2010.
[41] G. B. Arfken and H. J. Weber, *Mathematical Methods for Physicists*. Burlington, MA, USA: Academic Press, 2005.
[42] B. Girod, R. Rabenstein, and A. Stenger, *Signals and Systems*. New York, NY, USA: Wiley, 2001.
[43] R. N. Bracewell, *The Fourier Transform and Its Applications*. New York, NY, USA: McGraw-Hill, 1986.
[44] R. Kennedy, P. Sadeghi, T. Abhayapala, and H. Jones, "Intrinsic limits of dimensionality and richness in random multipath fields," *IEEE Trans. Signal Process.*, vol. 55, no. 6, pp. 2542–2556, Jun. 2007.
[45] J. Ahrens and S. Spors, "An analytical approach to sound field reproduction with a movable sweet spot using circular distributions of loudspeakers," in *Proc. IEEE Int. Conf. Acoust., Speech, Signal Process.*, Taipei, Taiwan, 2009, pp. 273–276.
[46] N. Hahn, F. Winter, and S. Spors, "Local wave field synthesis by spatial band-limitation in the circular/spherical harmonics domain," in *Proc. Audio Eng. Soc. Conv.*, Paris, France, May 2016.
[47] F. Winter, F. Schultz, G. Firtha, and S. Spors, "A geometric model for prediction of spatial aliasing in 2.5 D sound field synthesis," *IEEE/ACM Trans. Audio Speech Lang. Process.*, vol. 27, no. 6, pp. 1031–1046, Jun. 2019.
[48] J. R. Driscoll and D. M. Healy, "Computing Fourier transforms and convolutions on the 2-sphere," *Adv. Appl. Math*, vol. 15, no. 2, pp. 202–250, 1994.
[49] N. Baddour, "Operational and convolution properties of three-dimensional fourier transforms in spherical polar coordinates," *J. Opt. Soc. Amer.*, vol. 27, no. 10, pp. 2144–2155, 2010.
[50] D. Schlichthärle, *Digital Filters*. Berlin, Germany: Springer, 2014.
[51] Wolfram Research, "Spherical Bessel function of the first kind," Accessed: Jul. 16, 2021. [Online]. Available: http://functions.wolfram.com/03.21.21.0038.01
[52] T. Stilson and J. O. Smith, "Alias-free digital synthesis of classic analog waveforms." in *Proc. Int. Comput. Music Conf.*, 1996.
[53] E. Brandt, "Hard sync without aliasing," in *Proc. Int. Comput. Music Conf.*, Havana, Cuba, 2001, pp. 365–368.
[54] V. Valimaki and A. Huovilainen, "Antialiasing oscillators in subtractive synthesis," *IEEE Signal Process. Mag.*, vol. 24, no. 2, pp. 116–125, Mar. 2007.
[55] T. I. Laakso, V. Valimaki, M. Karjalainen, and U. K. Laine, "Splitting the unit delay," *IEEE Signal Process. Mag.*, vol. 13, no. 1, pp. 30–60, Jan. 1996.
[56] V. Välimäki, J. Pekonen, and J. Nam, "Perceptually informed synthesis of bandlimited classical waveforms using integrated polynomial interpolation," *J. Acoust. Soc. Amer.*, vol. 131, no. 1, pp. 974–986, 2012.
[57] J. Kaiser and R. Schafer, "On the use of the $I_0 - \sinh$ window for spectrum analysis," *IEEE Trans. Acoust. Speech Signal. Process.*, vol. 28, no. 1, pp. 105–107, Feb. 1980.
[58] J. Nam, V. Valimaki, J. S. Abel, and J. O. Smith, "Efficient antialiasing oscillator algorithms using low-order fractional delay filters," *IEEE Trans. Audio Speech Lang. Process.*, vol. 18, no. 4, pp. 773–785, May 2010.
[59] N. Hahn and S. Spors, "Discrete time modeling of spherical harmonics expansion by using band-limited step functions," in *Proc. 46th German Annu. Conf. Acoust. (DAGA)*, Hannover, Germany, Mar. 2020, pp. 1188–1191.